

Modeling capabilities on the formation of contrails in a commercial CFD code

Sébastien Cantin¹, François Morency² and François Garnier³

Sebastien.cantin.1@ens.etsmtl.ca

Department of Mechanical Engineering

Ecole de technologie supérieure

Montréal

Canada

ABSTRACT

Aircraft contrails may contribute to the global radiative forcing. In this context, the investigation of contrail formation in the near field of an aircraft engine may be helpful in developing numerical models to reduce undesirable impacts. This study is based on three-dimensional CFD simulations with an ice microphysics module in order to investigate the ice particles formation and evolution behind a complex geometry of an aircraft engine involving a bypass and a core flow. The Unsteady Reynolds-Averaged Navier-Stokes equations are used to model the flow. Particles emitted from the engine are tracked with a Lagrangian approach accounting for ice particles growth. The simulations were carried out under realistic operation conditions for two aircraft engines: the CFM56-3 and the LEAP-1A, a recent one. The model can differentiate the formation threshold of ice particles between both engines (26 % earlier in term of distance for the LEAP-1A). Then, larger mean ice particles are found at the end of the simulation for the LEAP-1A (20 % larger). Finally, the results show that the optical depth is higher for the CFM56-3 (360 % higher).

Keywords: contrails; CFD, engine jet, ice particles growth

NOMENCLATURE

AIC	Aircraft Induced Cirrus
AFR	Air Fuel Ratio
LES	Large Eddy Simulation
PDF	Probability Density Function
RANS	Reynolds Average Navier-Stokes

Symbols

D	Bypass diameter
λ_l	Wavelength to visible light
N	Dilution ratio
μ_r	Refractive index for ice
ρ	Density
P	Pressure
P_w	Water vapour partial pressure
P_w^0	Water vapour saturation
Q_{ext}	Mie extinction efficiency
r	Radius
S	Saturation ratio
T	Temperature
τ_v	Optical depth
U_{cl}	Centerline velocity
Y	Mass fraction
Z	Passive scalar

Subscripts

a	Air
g	Gas
p	Particle
w	Water vapour

1.0 INTRODUCTION

The passenger transport by commercial aviation knows an approximately constant 5 % growth per year [1]. This growth may have a critical effect on the climate. One consequence is the expected increase of Aircraft Induced Cirrus (AIC), that result from the long persistence of condensation trails (contrails) in the atmosphere and participate in the radiative forcing [2]. The knowledge of processes and key factors that control the ice particles formation in the initial stage are crucial to model and predict the initial properties of AIC [3].

In flight condition, soot particles and water vapour emitted from aircraft engines are mixed with the ambient air. The mixing process makes the core flow cool and increases the water vapour saturation ratio in the plume. Under favourable atmospheric conditions, microphysical processes take place such as heterogeneous freezing of water vapour onto soot particles and lead to the formation of contrails [4]. Then, the particles released by the engines are trapped into the vortex sheet shed by the wings, which rolls up into a pair of counter-rotating vortices to form the aircraft wake [5].

Modelling contrail formation in the engine near field is particularly complex since it involves multi-scale phenomena, such as compressible mixing, two-phase flow, turbulence mixing and microphysics. Single-parcel models, which include detailed chemical reactions and detailed microphysics, have been used in previous studies [6, 7]. These studies use average dilution to compute detailed characterizations of ice particles in terms of size and distribution. The average dilution leads to some discrepancies with in situ measurements due to the absence of a detailed turbulence modelling [8] or leads

to a simplified modelling of the jet dynamics that does not take into account the bypass and the core flow [9]. Computational Fluids Dynamics has demonstrated its abilities to model contrails with various models: RANS [10], LES [5, 11], LES coupled with detailed microphysics/complex chemistry model [12, 13]. In these studies, none of them are taking into account the aircraft engine involving a bypass and a core flow.

In this paper, we propose a URANS CFD model coupled with a microphysics model to study the ice particles formation in a plume using aircraft engine complex geometries involving bypass and core flow. The flows are computed behind the CFM56-3 and the recent LEAP-1A. The microphysics model has been implemented in the commercial software STAR-CCM+.

The paper is organized as follows. Section 2.0 describes the problem and the computational domain. Section 3.0 describes the model equations for the flow dynamics and the ice microphysics. Section 4.0 exposes the numerical methods and the initial conditions for the two aircraft engines. Section 5.0 compares the results between two aircraft engines regarding the verification of the plume dilution. Finally, the ice microphysics results are presented.

2.0 PROBLEM DEFINITION

At 35 000 feet, the flow downstream of an aircraft engine is composed of a hot air core flow and a bypass flow surrounding the core flow that promotes the mixing. The core flow emits water and soot particles in a cold and moist ambient air. These two flows are mixed with the free stream flow. Ice particles can be formed if the saturation inside the plume is high enough. Figure 1 shows a simplified scheme of the problem. The hot core flow contains two gas phases (air and water vapour) and a solid phase (soot particles). The free stream and the bypass flow are composed of air and water vapour.

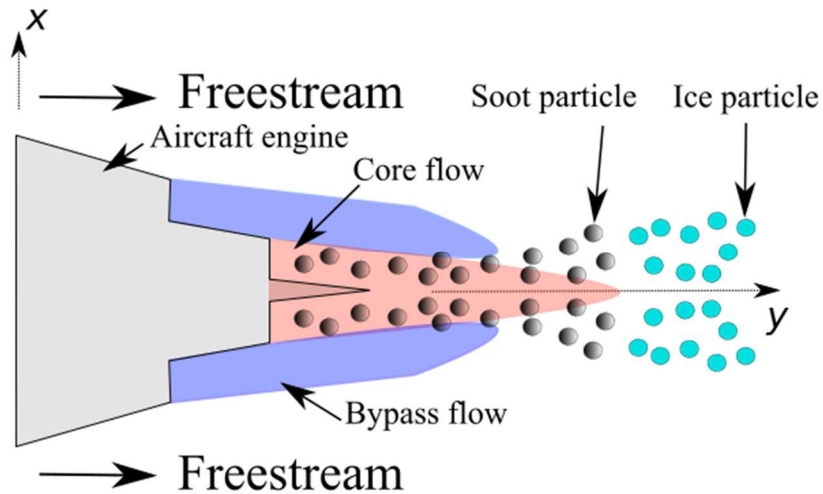


Figure 1 Scheme of the problem

Characterization of soot particles, exhaust thermodynamic conditions and geometry specifications are different for both engines (CFM56-3 and LEAP-1A). The gas phase is modelled with an Eulerian approach whereas the particle tracking (soot and ice particles) is made with a Lagrangian approach. A one-way coupling is considered between the gas and the solid phases. Furthermore, in this work, the particle drag is neglected and only the mass exchange between the solid phase and the gas phase is considered [11]. In the following section, the mathematical models for the flow are presented.

3.0 GOVERNING EQUATIONS

The flow is modelled with the STAR-CCM+ commercial code solver. First, the equations used to predict the fluid motion are described. Secondly, the equation to track

the particle motion is presented. Finally, the microphysical model added to the solver to describe the ice particle growth is presented.

3.1 Gas phase equations

The gas phase (index $_g$) is composed of two species, the air (index $_a$) and the water vapour (index $_w$) produced by the combustion. The gas phase is assumed to be an ideal gas. The gas pressure p_g is calculated from $p_g = \rho_g R T_g$ where ρ_g is the gas density, T_g is the gas temperature and R is the specific gas constant. The Unsteady Reynolds-Averaged Navier-Stokes (URANS) equations are used to model the flow motion and turbulence. As the calculation of ice particles growth is time-dependent, the flow is assumed to be unsteady. For compressible flow, a density-weighted decomposition on ensemble averages is used; the variables are then defined as $\tilde{\Phi} = \bar{\rho}\Phi/\bar{\rho}$ and $\Phi = \tilde{\Phi} + \Phi''$. The following equations are written in Cartesian coordinates ($O, \tilde{x}, \tilde{y}, \tilde{z}$). The flow is considered Newtonian. The Reynolds stresses are modelled by the Boussinesq hypothesis. The mass-conversation of air (Equation (1)) and water vapour (Equation (2)) species are given below:

$$\frac{\partial}{\partial t}(\bar{\rho}_w \tilde{Y}_w) + \nabla \cdot (\bar{\rho}_w \tilde{Y}_w \tilde{u}) - \nabla \cdot \left(\left(D_v + \frac{\mu_t}{\sigma_t} \right) \nabla \tilde{Y}_w \right) = -n \bar{m}_p \quad (1)$$

$$\frac{\partial}{\partial t}(\bar{\rho}_a \tilde{Y}_a) + \nabla \cdot (\bar{\rho}_a \tilde{Y}_a \tilde{u}) - \nabla \cdot \left(\left(D_a + \frac{\mu_t}{\sigma_t} \right) \nabla \tilde{Y}_a \right) = 0 \quad (2)$$

where \tilde{u} is the mean velocity. The variables $\bar{\rho}_w$, D_w , \tilde{Y}_w and $\bar{\rho}_a$, D_a , \tilde{Y}_a are the density, the molecular diffusivity, the mass fraction of water vapour and air respectively, σ_t denotes the turbulent Schmidt number. The dynamic viscosity for gas μ_g is defined as $\mu_g = \mu_m + \mu_t$ where μ_m stands for the molecular viscosity and μ_t for the turbulent viscosity defined as $\mu_t = \bar{\rho}_g k \tau_s$ where k and τ_s are the turbulent kinetic energy and the turbulent timescale respectively. The mass transfer \bar{m}_p between water vapour (gas) and ice particles (solid) has been implemented in the software. It is detailed in the next section. The number density of particles contained in a volume cell V is n where $n = N/V$, N particles in a volume cell V . The Standard $k - \varepsilon$ turbulence model is used since it has demonstrated its ability to model a compressible coaxial jet [14].

3.2 Particles motion

In this study, particles are represented by soot and ice particles. These latter are tracked individually by a Lagrangian approach. Because the number density of soot particles is high (of the order of 10^{11} m^{-3} in cruise condition according to [15]), we minimize the simulation cost by carrying on computational particles, each representing N physical particles. These latter can be considered spherical [16], with a radius r_p . They are treated as passive tracers due to their small size (sub-micron). Thus, they have the same velocity as the carrier phase and the drag and gravity forces are neglected. The particle relaxation time is small (of the order of 10^{-5} s for ice particles with the largest r_p of a few microns) and negligible, as compared to the flow characteristic time [17]. The particles movement is then governed by the following equation:

$$\frac{dx_p}{dt} = \tilde{u}(x_p) \quad (3)$$

where \tilde{u} is the mean velocity at x_p , the particle position.

3.3 Ice microphysical model

The initial state of the contrail particles is liquid, but because of the very low local temperature and the presence of soot particles, heterogeneous freezing takes place and spherical-shaped ice particles form [18]. A saturation ratio larger than 1 above a flat surface of pure water is therefore required for contrails to form [19]. The saturation ratio S , is defined as:

$$S = \frac{P_w(T)}{P_w^0(T)} \quad (4)$$

where P_w is the water vapour partial pressure, and P_w^0 is the water vapour saturation pressure.

Moreover, heterogeneous ice nucleation rates are not explicitly calculated. When the gas temperature reaches a threshold value, all the particles considered in a grid cell are assumed to freeze and, are therefore treated as ice particles. The size of ice particles (spherical shape) varies as a function of the jet temperature and relative humidity. The net mass change per particle due to condensation and evaporation effects is determined by solving the condensation Equation [20]:

$$\frac{dm_p}{dt} = \frac{4\pi r_p (S-A)}{\frac{L^2 M_w}{k_g R T_p f_{3\alpha}} A + \frac{R T_p}{P_w^0 D_w M_w f_{3\beta}}} \quad (5)$$

where m_p denotes the mass of the particle, and D_w indicates the water vapour diffusivity in the air. L , M_w , and k_g represent the latent heat of condensation of water vapour, the molecular weight of water vapour and the thermal conductivity of gas respectively. The particles temperature T_p is obtained as the local, instantaneous, gas phase variables, and is assumed to be equal to the gas temperature T_g because the particles (soot and ice particles) are supposed to be in equilibrium with the carrier gas (i.e., $T_p \approx T_g$). $f_{3\alpha}$ is a correction factor for temperature difference between the boundary layer and the ambient air, and $f_{3\beta}$ is a correction factor for the new vapour density difference with respect to the old Maxwell type model. Equation (5) can be rearranged to obtain the net rate of change of the particle size:

$$\frac{dr_p}{dt} = \frac{(S-A)}{\frac{L^2 M_w \rho_p}{k_g R T_p^2 f_{3\alpha}} A + \frac{R T_p \rho_p}{P_w^0 D_w M_w f_{3\beta}}} \frac{1}{r_p} \quad (6)$$

where ρ_p is the particle density, and A describes the Kelvin effect and is defined as the ratio of the vapour pressure at the water droplet surface (before freezing) to the saturated vapour pressure over a flat surface at the droplet temperature. More details about the model are available in [20].

Thus, we obtain the mass variation of each ice particle and a fortiori vapour mass variation, which leads to the coupling term of Equation (7). The term \overline{m}_p is given by the relation:

$$\overline{m}_p = \frac{d}{dt} \left(\frac{4}{3} \rho_p \pi r_p^3 \right) \quad (7)$$

4.0 NUMERICAL METHODS AND INITIAL CONFIGURATION

In this section, we present the numerical methods. Details about the geometry and the meshes of both engines investigated in this study are given. A short paragraph explains the numerical method used. Then, we present the microphysical code algorithm. Finally, the last sub-section summarizes the initial configuration parameters and the boundary conditions for the computational domain.

4.1 Geometry

Both engines have a core flow and a bypass flow, as identified in Figure 2. One feature of the computational domain is that only one quarter of the engine was used. In this work, we focus on the jet propellant, so only the engine rear body was considered.

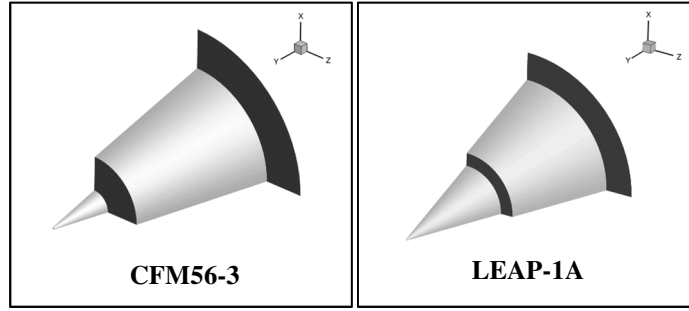


Figure 2 Schematic drawings for the CFM56-3 on the left and for the LEAP-1A on the right

The computational domain has a radius $R = 5D_i$ (where D_i denotes the bypass outer diameter, either $D_{b,CFM}=1.586$ m for the CFM56-3 or $D_{b,LEAP}=2.200$ m for the LEAP-1A) and a length $L = 100D_i$. The length L was fixed to this value in order to follow the evolution of the ice particles until 0.5 s behind the engine.

4.2 Meshes

The geometries for both aircraft engine have been meshed using ICEM-CFD. Figure 3 shows the meshes for the CFM56-3 and for the LEAP-1A. The 180° figures are produced to ease the visualization of the meshes. The resulting meshes consist of 7 million of cells for both engines. Multiblock meshes were generated containing hexahedral elements to solve the jet shear layer and the core region. The mesh is particularly well refined where velocity and pressure gradients are expected to be high (i.e. at the engine exhaust and in the shear layer). Moreover, the mesh is refined near the wall to reach a maximum y^+ nearly equal to 5 and wall law is employed to model the boundary layer. A maximum growth rate of 1.25 between the nodes near the wall is employed. The tips of both engines were cut to prevent the formation of skewed grid cells. The far field mesh in the radial direction is coarser since gradients are expected to be lower than in the region behind the engine.

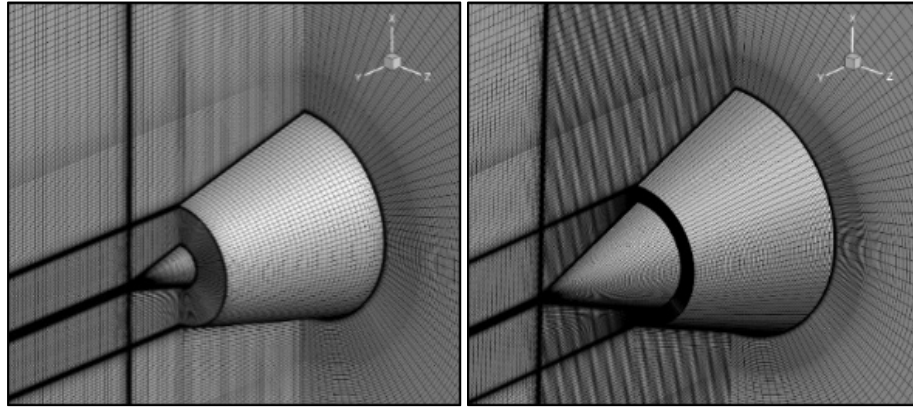


Figure 3 Computational meshes for the CFM56-3 on the left and for the LEAP-1A on the right

4.3 Numerical methods

The numerical method is based on a cell-centered finite volume approach, and a pseudo-time approach is used through a coupled flow solver for compressible flow. A Courant Friedrich Number (CFL) of 1 was set. The fluid and turbulence equations are solved by a second-order accurate upwind scheme in space and by a second-order accurate Euler scheme for time integration. The time step is set to 10^{-3} s. Equation (7) for the particle radius is solved with a fourth-order Runge-Kutta scheme. To initialize the calculation, a grid sequencing method was used. The sequenced results are then interpolated onto the finer grid for continued processing. One level of sequencing involves removing every other grid point from the previous level. The solution started at two levels of sequencing and progressed to the full grid solution.

A two-step methodology is used to obtain the results. In the first step, the flow composed of air and water is first simulated with a steady-state approach. Convergence is determined once the average residuals of the continuity, momentum, energy, turbulent kinetic energy and turbulent dissipation rate equations decrease at least four orders of magnitude. The mass flow and the thrust of both engines are also monitored to assess the convergence of the simulation. Then, we switch to the unsteady approach. The motion of the particles and ice particle growth as a function of time are calculated as well as the gas phase equations. The following sub-section describes the ice microphysical module implemented into STAR-CCM+.

4.4 Ice microphysical module

The ice microphysical module is based on the mathematical model of [20] presented in the previous section 3.0. The code is composed of 2 files implemented in C language. One file is dedicated to the computation of the particle radius growth (Equation (6)). The other file aims to compute the mass source term (Equation (5)). In this paper, we only detail the algorithm of the main file that calculates the particle radius growth (see Figure 4).

At the beginning of the module, the thermodynamic variables are collected from STAR-CCM+. Then, at the first time step, the particle radius is initialized in an array according to a log-normal distribution. For other time steps, the previous particle radius is obtained from a CSV file saved by STAR-CCM+ and stored in a buffer. After that, the module checks the residence time for each particle. For new particles, the radius is initialized. For particles already emitted, the radius at the previous time step is found in the buffer. The thermodynamics variables (saturation ratio, water vapour partial pressure, conductivity of air...) are computed then, and the module evaluates the saturation ratio for each particle. For saturated particles, a new particle radius is calculated with the Equation (6). On the other hand, non-saturated particles keep identical radius. Finally, once all the particles have been evaluated, all their radius are returned to STAR-CCM+.

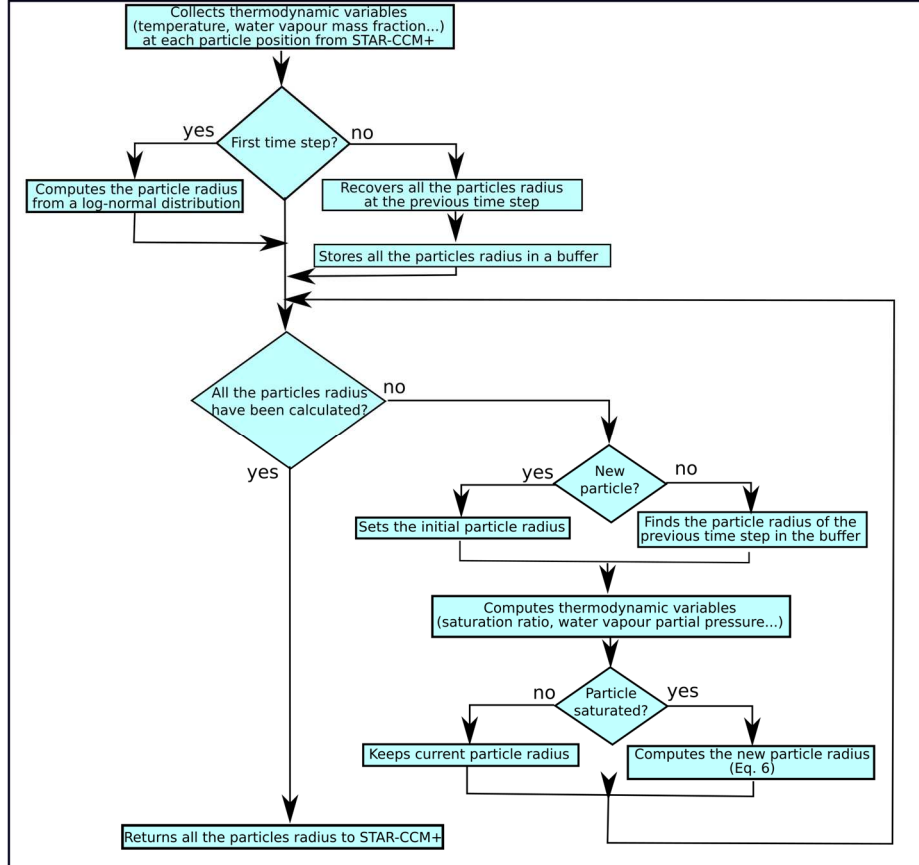


Figure 4 Algorithm of the microphysical code

4.5 Initial and boundary conditions

In this sub-section, we present the thermodynamics set-up, the soot particle initialization and the boundary conditions.

4.5.1 Thermodynamics set-up

The initial flow configuration is based on an aircraft flight at a cruise altitude to allow water vapour to condense onto soot particles and form ice particles. The flow around the aircraft engine is set at a speed of 252 m.s^{-1} , a static temperature of 219 K , and a static pressure of $23\,800 \text{ Pa}$, representing the ambient condition at $35\,000 \text{ ft}$ [21]. Also, the water vapour molar fraction is fixed at 6.08×10^{-5} to reach an ambient relative humidity of 60% . The initial molar fraction for water vapour was set to 2.2×10^{-2} for both engines. The initial thermodynamics conditions for the CFM56-3 [21] and for the LEAP-1A engines are given on Table 1. A turbulence intensity of 10% was imposed as a turbulence initial condition for both engines, as it was done previously by [21].

Table 1
Engine initial conditions

Engine type	CFM56-3	LEAP-1A
Core flow: Mach	1	1
Total Pressure (Pa)	45 430	39 310
Total Temperature (K)	696	637
Bypass flow: Mach	1	1
Total Pressure (Pa)	60005	50 000
Total Temperature (K)	290	278

4.5.2 Soot particle initialization

The particle injection is defined as a particle stream. One shot of particles is emitted from the engine at the beginning of the simulation and has been tracked at each time step of the simulation. The soot particle distribution for both engine exits is polydisperse. All the particles emitted have a different radius. The probability distribution law is a lognormal as it is referred in experimental studies [22]. A log-normal distribution [23] implemented into STAR-CCM+ enable the setting of the particles radius range.

The initial diameter for the soot particle emitted by the CFM56-3 is set at 25 nm with a standard deviation of 1.6 , according to in situ measurement from [24]. The particle emission index is measured at $PEI_p = 4 \times 10^{14}$ particles per kg of fuel. This gives a particle number of $n = (PEI_p \times \rho_{core}) / (AFR + 1) \approx 9.44 \times 10^{11} \text{ \#} \cdot \text{m}^{-3}$ with $\rho_{core} = 0.144 \text{ kg} \cdot \text{m}^{-3}$. Based on the numerical study for a CFM56-3 of [25], we set the number particles soot at $n = 10^{12} \text{ \#} \cdot \text{m}^{-3}$.

For the LEAP-1A, no experimental data about soot initial conditions are available yet. A recent study compared particulate matter emissions of modern engines (SAM146 and CFM56-7B26/3) and shows that the geometric mean diameter (15.2 nm) and the geometric standard deviation (1.49) are almost the same for both engines [22]. The soot particle number is estimated by the particulate matters number emitted by the new combustor chamber from the LEAP-1A. Modern engines tend to emit fewer soot particles than older one (90% of reduction according to [26]). Hence, we decide to set the number of soot particles at $n = 10^{11} \text{ \#} \cdot \text{m}^{-3}$ for the LEAP-1A. The soot initial conditions are shown on Table 2.

Table 2
Soot initial conditions

Engine type	CFM56-3	LEAP-1A
Geometric Mean Diameter (nm)	25	15.2
Geometric Standard Deviation	1.60	1.49
Number soot particle ($\text{\#} \cdot \text{m}^{-3}$)	10^{12}	10^{11}
Size distribution	Log normal	Log normal

4.5.3 Boundary conditions

Figure 5a) shows the 45-degree computational domain with the boundary conditions. At the inlet, the total pressure and the total temperature are set. The boundary conditions named outlet has a fixed static pressure and a static temperature. On each side of the cylinder, a symmetry boundary condition is set. Figure 5b) shows the boundary condition at the engine exhaust outlet. The total pressure and the total temperature are imposed for the core flow and bypass flow respectively. A no-slip condition is imposed on walls.

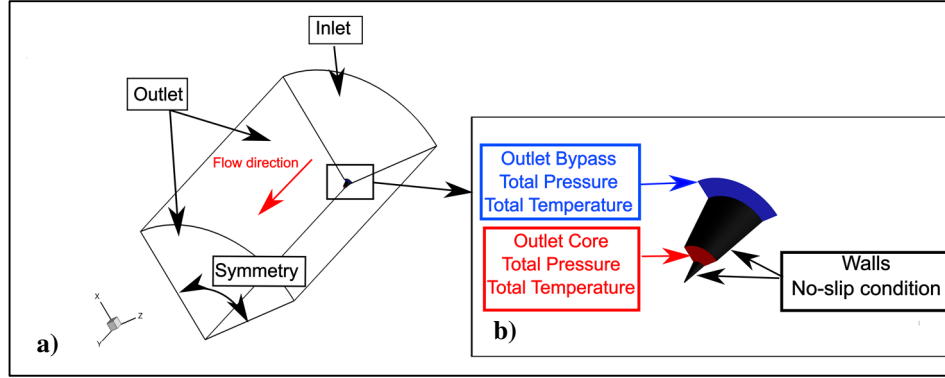


Figure 5 Boundary conditions of the computational domain a), with a close-up to the engine primary core (red) and bypass flow (blue) b)

5.0 RESULTS AND DISCUSSION

This section deals with the results obtained from the comparison of ice particle formation between two aircraft engines. This section is divided in two sub-sections, one for the validation of the mixing and dilution results and the other one about microphysical results.

5.1 Dilution flow validation

Figure 6 shows the dilution ratio N versus the plume age in the second. Our numerical results calculations are compared with the in-situ experimental results from [27]. The experimental results correspond to temperature and contrail diameter measurements. The dilution ratio N can be determined from the measured concentration (i.e. a passive scalar), temperature, and contrail diameter values using relationships more detailed in [28]. Then, the dilution ratio calculated from these values can be compared between each other. The dilution ratio N is calculated from the dilution of a passive scalar Z :

$$N = \frac{AFR}{Z} \quad (8)$$

where N is the dilution ratio, AFR is known as the Air Fuel Ratio and Z is the ratio of the amount of fluid from the jet region to that from the free stream. Then, the ratio Z [21] is calculated from:

$$\tilde{Z} = \frac{\tilde{Z}_i - \tilde{Z}_{i,atm}}{\tilde{Z}_{i,jet} - \tilde{Z}_{i,atm}} \quad (9)$$

where \tilde{Z}_i is the concentration of a species at any point in the solution, $\tilde{Z}_{i,atm}$ is the initial atmospheric concentration of the species and $\tilde{Z}_{i,jet}$ denotes the initial jet concentration. The concentration measurement is taken along the jet axis. As our simulations are spatial, we related the distance behind the aircraft to the time by the velocity along the jet axis:

$$t = \frac{\tilde{Z}}{\tilde{u}_{cl}} \quad (10)$$

The validation of numerical results with in-situ measurements is challenging because the measurements give only a rough estimate of the bulk mean concentration [28]. The measuring aircraft will have missed some peak concentration positions. This may cause a possibly large overestimate of the dilution ratios. On the other hand, incidental encounters of maximum peak concentrations may result in a relatively small underestimate of the bulk dilution. However, experimental and numerical results have the same order of magnitude as shown in Figure 6. Consequently, we assume that the simulated plume is sufficiently accurate for suitably computation of microphysical processes in the wake of the jet propellant.

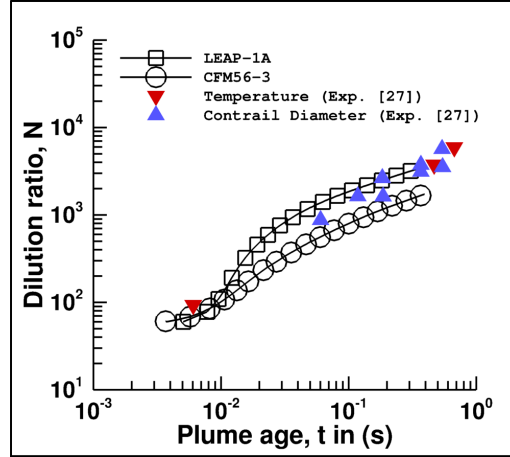


Figure 6 Comparison of the dilution ratio of a passive scalar simulated from the CFM56-3 and the LEAP1A with in-situ measurements

5.2 Microphysical results

Figure 7 shows the saturation iso-contours where ice particles are identified with white points.

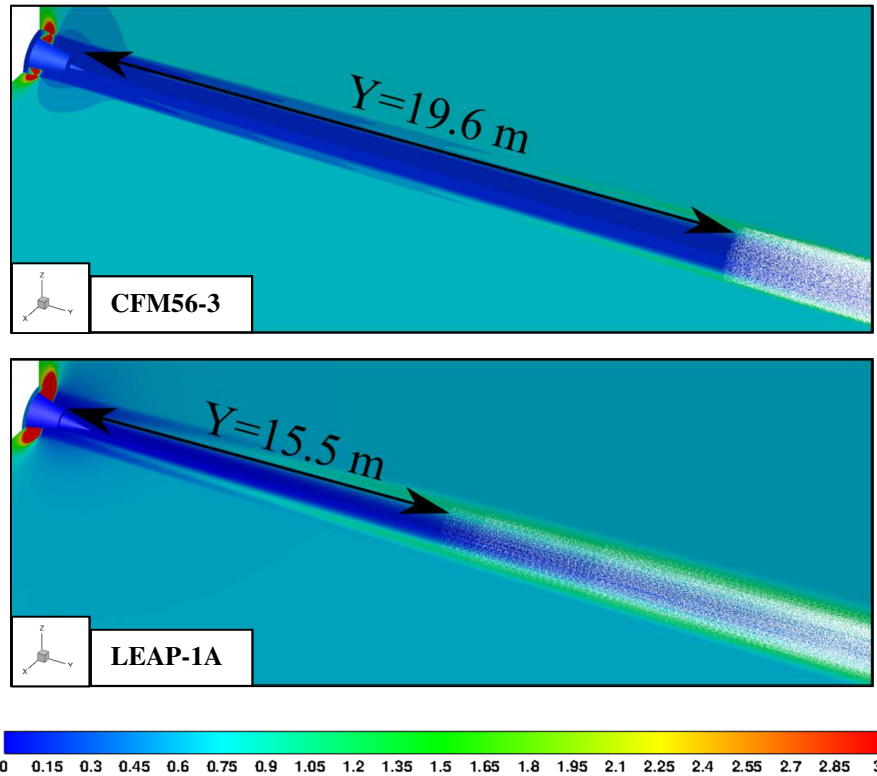


Figure 7 Iso-contours of the saturation ratio with ice particles (white) for both aircraft engines

Near the engine, the saturation ratio is high (red color). Shocks appears near the exhaust since a Mach number of 1 is reached. So, the absolute total pressure increases strongly. This causes an increase of the water vapour partial pressure since this latter depends on the absolute total pressure. Then, the absolute total pressure drops and returns to a steady-state close to the ambient absolute total pressure. Downstream of both engines, ice particles cannot be formed since the temperature in the plume is still high to allow ice particles formation. The saturation vapour pressure of liquid water is still too low (i.e. $S < 1$). The edge of the jet starts to cool earlier than the center of the jet where the hot and moist flow mixes with the cold and dry ambient air. Supersaturation conditions (i.e. $S > 1$) appear about $Y=19.6$ m for the CFM56-3 and about $Y=15.5$ m for the LEAP-1A. At these positions, ice particles form. This figure shows that our model can differentiate the delay of ice particles formation between two different aircraft engines (26 % earlier in term of distance for the LEAP-1A).

Figure 8 compares the evolution distance of the mean particle radius r_p^m for both engines. The mean particle radius is given by:

$$r_p^m = \frac{\sum_i r_{p,i}}{n_i} \quad (11)$$

where $r_{p,i}$ represents the particle radius inside the sub-domain i and n_i is the number of particles inside the sub-domain i . The mean radius remains constant near the engine exhaust and then start to increase significantly up to $2.0 \mu\text{m}$ for the LEAP-1A and up to $1.7 \mu\text{m}$ for the CFM56-3 at the end of the simulation. The difference is about 20 %. This confirms that the LEAP-1A forms particles of larger size. Figure 8 shows that ice particles are formed earlier with the LEAP-1A. This is relevant as compared with the results shown in Figure 7.

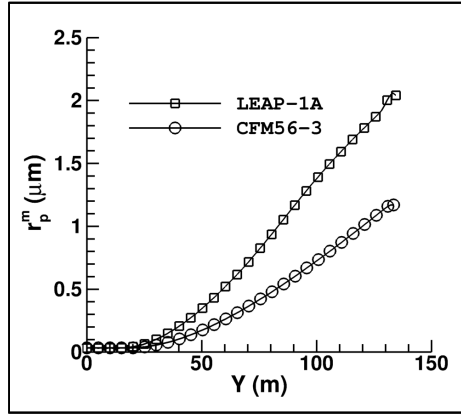


Figure 8 Comparison of the distance evolution of the mean particle radius

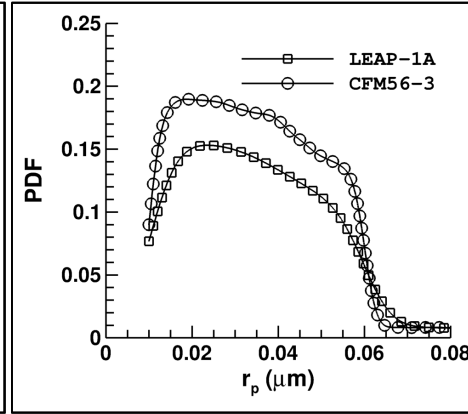


Figure 9 Comparison of the PDF of particles radius at $Y=30$ m

Figure 9 shows the Probability Density Function (PDF) of particle radius r_p at the position $Y=30$ m. The PDF peak was reached at a particle radius of $0.024 \mu\text{m}$ (PDF=0.15) and $0.018 \mu\text{m}$ (PDF=0.19) for the LEAP-1A and CFM56-3 cases, respectively. This shows that in the engine plume, larger particle sizes are formed in the LEAP-1A case.

Figure 10 shows the evolution of optical depth behind both engine aircraft. The optical depth characterizes contrail visibility [29] and is defined by:

$$\tau_v = \pi r_p^2 N Q_{ext}(r_p) \Delta z \quad (12)$$

where the Mie extinction efficiency Q_{ext} at a given wavelength λ_w is approximated by:

$$Q_{ext} = 2 - \frac{4}{e} \left[\sin(e) - \frac{1 - \cos(e)}{e} \right], \quad (13)$$

$$e = \frac{4\pi r_p(\mu_r - 1)}{\lambda_l} \quad (14)$$

where the refractive index $\mu_r = 1.31$ for ice and wavelength $\lambda_l = 0.55 \mu\text{m}$ corresponding to visible light. Δz denotes the characteristic length of the plume (i.e. the contrail thickness). The optical depth is evaluated as function of the non-dimensional value Y/D . Contrails are visible for the typical values where $\tau_v \geq 0.01$. In our case, contrails are visible at $Y=65.4 \text{ m}$ and $Y=46.6 \text{ m}$ for the LEAP-1A and CFM56-3, respectively. It means that the contrails are visible earlier for the CFM56-3. Moreover, the optical depth value goes up to 0.410 for the CFM56-3 and it goes up to 0.089 for the LEAP-1A at the end of the simulation. The difference is highly noticeable (360 % of difference) and can be attributed to the higher soot number initially ($\times 10^3$) emitted at the CFM56-3 exhaust considering its contribution in Equation (12). This causes a higher number of ice particles to be formed, hence a higher optical depth.

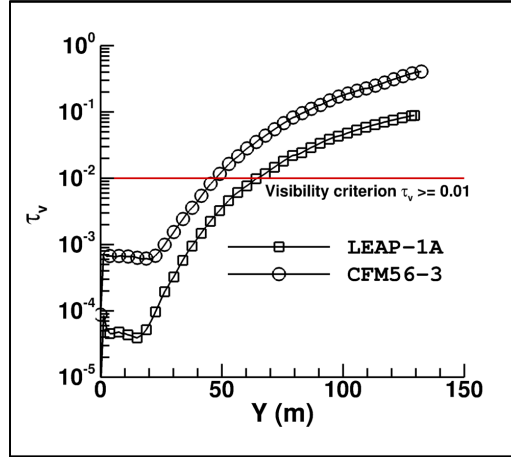


Figure 10 Comparison of the optical depth evolution with distance

6.0 CONCLUSION

In this study, we developed, for the first time, tri-dimensional CFD simulations with a microphysics module in order to investigate the ice particles formation and evolution behind a complex geometry of an aircraft engine involving a bypass and a core flow. The Unsteady Reynolds-Averaged Navier-Stokes equations were used to compute the flow. Particles emitted from the engine were tracked with a Lagrangian approach accounting for ice particle growth. The simulations were carried out under realistic operation conditions for two aircraft engines: the CFM56-3 and the recent LEAP-1A. The microphysics model has been implemented in the commercial software STAR-CCM+. Our results show the flow comparison between the two aircraft engines.

Results were first validated in term of the plume dilution characterizing the turbulent mixing throughout the engine jet. Good agreement is observed between the experimental and the numerical results since our data have the same order of magnitude as the measurements. Consequently, we assumed that the simulated plume is sufficiently accurate for suitably computing microphysics processes in the wake of the jet propellant.

Then, the results show that the saturation ratio seems to be higher in the jet flow for the LEAP-1A compared to the CFM56-3. This promotes earlier ice particles formation. As a consequence, ice particles are formed earlier for the LEAP-1A (26 % earlier in term of distance) compared to the CFM56-3. Also, the mean ice particle radius is quantitatively higher at the end of the simulation in the case of the LEAP-1A. The difference is about 20 %. We also compared the PDF of ice particles radius at $Y=30 \text{ m}$. Results show that near the engine, larger size particles are formed in a smaller proportion (PDF=0.15 with a particles radius of $0.024 \mu\text{m}$) in the LEAP-1A case. Finally, the optical depth was compared. Contrails are visible for the typical values where $\tau_v \geq 0.01$. In our case,

contrails are visible at $Y=64.5$ m and $Y=46.6$ m for the LEAP-1A and CFM56-3, respectively. The contrails are visible earlier for the CFM56-3. Moreover, the optical depth values are higher (360 %) for the CFM56-3 compared to the LEAP-1A at the end of the simulation. This can be attributed mainly to the higher soot number initially emitted at the CFM56-3 exhaust that causes a higher optical depth.

ACKNOWLEDGMENTS

This research was enabled in part by support provided by Calcul Québec (www.calculquebec.ca/) and Compute Canada (www.computecanada.ca/).

REFERENCES

- [1] ICAO, "ICAO Environmental Report 2017," 2017.
- [2] BURKHARDT, U. AND B. KÄRCHER, "Global radiative forcing from contrail cirrus." *Nature Climate Change*. 1, (1): p. 54-58, 2011.
- [3] KÄRCHER, B., "Formation and radiative forcing of contrail cirrus." *Nature communications*. 9, (1): p. 1824, 2018.
- [4] KÄRCHER, B., "Physicochemistry of aircraft-generated liquid aerosols, soot, and ice particles: 1. Model description." *Journal of Geophysical Research: Atmospheres*. 103, (D14): p. 17111-17128, 1998.
- [5] PAOLI, R., L. NYBELEN, J. PICOT AND D. CARIOLLE, "Effects of jet/vortex interaction on contrail formation in supersaturated conditions." *Physics of Fluids*. 25, (5): p. 053305, 2013.
- [6] KÄRCHER, B. AND F. YU, "Role of aircraft soot emissions in contrail formation." *Geophysical Research Letters*. 36, (1): p. L01804 (5 pp.), 2009.
- [7] WONG, H.-W., M. JUN, J. PECK, I.A. WAITZ AND R.C. MIAKE-LYE, "Detailed Microphysical Modelling of the Formation of Organic and Sulfuric Acid Coatings on Aircraft Emitted Soot Particles in the Near Field." *Aerosol Science and Technology*. 48, (9): p. 981-995, 2014.
- [8] ROJO ESCUDE-COFINER, C., "Environmental impact of aircraft-produced aerosols : modelling and application of alternative fuels," Université de Strasbourg, 2012.
- [9] KÄRCHER, B., U. BURKHARDT, A. BIER, L. BOCK AND I.J. FORD, "The microphysical pathway to contrail formation." *Journal of Geophysical Research: Atmospheres*. 120, (15): p. 7893-927, 2015.
- [10] GUIGNERY, F., E. MONTREUIL, O. THUAL AND X. VANCASSEL, "Contrail microphysics in the near wake of a realistic wing through RANS simulations." *Aerospace Science and Technology*. 23, (1): p. 399-408, 2012.
- [11] GARNIER, F., E. MAGLARAS, F. MORENCY AND X. VANCASSEL, "Effect of Compressibility on Contrail Ice Particle Growth in an Engine Jet." *International Journal of Turbo & Jet-Engines*. 31, (2): p. 131, 2014.
- [12] VANCASSEL, X., P. MIRABEL AND F. GARNIER, "Numerical simulation of aerosols in an aircraft wake using a 3D LES solver and a detailed microphysical model." *International Journal of Sustainable Aviation*. 1, (2): p. 139-159, 2014.
- [13] PAOLI, R., X. VANCASSEL, F. GARNIER AND P. MIRABEL, "Large-eddy simulation of a turbulent jet and a vortex sheet interaction: Particle formation and evolution in the near field of an aircraft wake." *Meteorologische Zeitschrift*, 2008.
- [14] CANTIN, S., "Simulation numérique de la formation des traînées de condensation dans le champ proche d'un turboréacteur d'avion." Mechanical Department, Ecole de technologie supérieure, Montréal: p. Pages, 2018.
- [15] SCHUMANN, U., F. ARNOLD, R. BUSEN, J. CURTIUS, B. KÄRCHER, A. KIENDLER, K.H. WOHLFROM, "Influence of fuel sulfur on the composition of aircraft exhaust plumes: The experiments SULFUR 1-7." *Journal of Geophysical Research: Atmospheres*. 107, (D15): p. AAC 2-1-AAC 2-27, 2002.

- [16] SCHRÖDER, F., B. KARCHER, C. DUROURE, J. STROM, A. PETZOLD, J.F. GAYET, S. BORRMANN, "On the transition of contrails into cirrus clouds." *Journal of the Atmospheric Sciences*. 57, (4): p. 464-80, 2000.
- [17] PAOLI, R., J. HÉLIE AND T. POINSOT, "Contrail formation in aircraft wakes." *Journal of Fluid Mechanics*. 502: p. 361-373, 2004.
- [18] BURKHARDT, U., B. KÄRCHER AND U. SCHUMANN, "Global Modelling of the Contrail and Contrail Cirrus Climate Impact." *Bulletin of the American Meteorological Society*. 91, (4): p. 479-484, 2010.
- [19] JENSEN, E.J., O.B. TOON, S. KINNE, G.W. SACHSE, B.E. ANDERSON, K.R. CHAN, R.C. MIAKE-LYE, "Environmental conditions required for contrail formation and persistence." *Journal of Geophysical Research*. 103, (D4): p. 3929-36, 1998.
- [20] FUKUTA, N. AND L.A. WALTER, "Kinetics of Hydrometeor Growth from a Vapor-Spherical Model." *Journal of the Atmospheric Sciences*. 27, (8): p. 1160-1172, 1970.
- [21] GARNIER, F., C. BAUDOUIN, P. WOODS AND N. LOUISNARD, "Engine emission alteration in the near field of an aircraft." *Atmospheric Environment*. 31, (12): p. 1767-1781, 1997.
- [22] DELHAYE, D., F.-X. OUF, D. FERRY, I.K. ORTEGA, O. PENANHOAT, S. PEILLON, .D. GAFFIE, "The MERMOSE project: Characterization of particulate matter emissions of a commercial aircraft engine." *Journal of Aerosol Science*. 105: p. 48-63, 2017.
- [23] MAGLARAS, E., "Application de la simulation numérique des grandes échelles à la formation des traînées de condensation dans le sillage d'un avion." Mechanical Department, Université Bordeaux 1, Bordeaux: p. Pages, 2007.
- [24] SCHRÖDER, F., C.A. BROCK, R. BAUMANN, A. PETZOLD, R. BUSEN, P. SCHULTE AND M. FIEBIG, "In situ studies on volatile jet exhaust particle emissions: Impact of fuel sulfur content and environmental conditions on nuclei mode aerosols." *Journal of Geophysical Research: Atmospheres*. 105, (D15): p. 19941-19954, 2000.
- [25] KHOU, J.C., W. GHEDHAIFI, X. VANCASSEL AND F. GARNIER, "Spatial Simulation of Contrail Formation in Near-Field of Commercial Aircraft." *Journal of Aircraft*, 2015.
- [26] LEE, D.S., G. PITARI, V. GREWE, K. GIERENS, J.E. PENNER, A. PETZOLD, . . . R. SAUSEN, "Transport impacts on atmosphere and climate: Aviation." *Atmospheric Environment*. 44, (37): p. 4678-4734, 2010.
- [27] SCHUMANN, U., J. STRÖM, R. BUSEN, R. BAUMANN, K. GIERENS, M. KRAUTSTRUNK, J. STINGL, "In situ observations of particles in jet aircraft exhausts and contrails for different sulfur-containing fuels." *Journal of Geophysical Research: Atmospheres*. 101, (D3): p. 6853-6869, 1996.
- [28] SCHUMANN, U., H. SCHLAGER, F. ARNOLD, R. BAUMANN, P. HASCHBERGER AND O. KLEMM, "Dilution of aircraft exhaust plumes at cruise altitudes." *Atmospheric Environment*. 32, (18): p. 3097-3103, 1998.
- [29] JANSEN, J. AND A.J. HEYMSFIELD, "Microphysics of Aerodynamic Contrail Formation Processes." *Journal of the Atmospheric Sciences*. 72, (9): p. 3293-3308, 2015.